On the Impact of Build Envelope Sizes on E-PBF Processed Pure Iron

C.J.J. TORRENT, P. KROOß, and T. NIENDORF

In additive manufacturing, the thermal history of a part determines its final microstructural and mechanical properties. The factors leading to a specific temperature profile are diverse. For the integrity of a parameter setting established, periphery variations must also be considered. In the present study, iron was processed by electron beam powder bed fusion. Parts realized by two process runs featuring different build plate sizes were analyzed. It is shown that the process temperature differs significantly, eventually affecting the properties of the processed parts.

https://doi.org/10.1007/s11663-021-02368-3

IN powder bed-additive manufacturing (PB-AM), the product performance highly depends on a wide range of processing parameters. As is well known, the parameters (scanning strategy, beam deflection, hatch, intensity, layer thickness, *etc*.) have a pronounced impact.[1–6] Furthermore, unfrequently considered factors such as powder quality (sphericity, flowability, size distribution, *etc*.)[7, 8] and the part geometry[9] contribute to the microstructural evolution during processing. All aforementioned variables have a significant impact on the resulting process temperature and, thus, on the microstructure. This becomes particularly clear when the influence of specimen height[10] and specimen position on the build plate[11] are assessed. Consequently, many interrelated effects have to be taken into account in order to understand their impact on the resulting microstructure and mechanical properties. In PB-AM related research, especially in academic environments, various modifications are realized in the AM machines. For instance, in many cases only small material amounts are processed in AM machines originally designed for large volumes. Therefore, a reduction of the build envelope is required. In turn, established parameter settings can result in a differing behavior of the powder material, the melt, and the solidification path, respectively, if modifications of specific environments are ignored. However, studies detailing the influence of variations in the machine periphery, *e.g*., the size of the build envelope, are rare in literature. The present study tackles this research gap by focusing on the impact of different build envelope sizes on the final material properties.

In PB-AM, the local temperature history of a specific volume element of the build is referred to as *intrinsic*[12] or *in situ heat treatment*.[13] Repeated phase transformations can lead to grain refinement.[12] Consequently, a targeted design of the thermal level during processing can promote pronounced changes in microstructure evolution. As stated above, factors which influence the thermal conditions during processing are manifold and have to be characterized with respect to their impact on the material properties.

As a potential biodegradable implant material, commercially pure iron (cp-Fe) was processed via electron beam powder bed fusion (E-PBF) in a recent publication.[14] It was shown that an overall process temperature level below the phase transformation temperature ($\gamma \leftrightarrow \alpha$) leads to a microstructure dominated by low-angle grain boundaries (LAGB). In the present work, identical process parameters were applied to manufacture the same type of specimens on the same E-PBF system; however, a different build envelope size was used. It is revealed that these specimens differ significantly in terms of microstructure and mechanical response.

For present investigations, cp-Fe powder with a particle size range of 63 to 150 μm was processed using the E-PBF system ARCAM A2X (ARCAM AB, Mölndal, Sweden). 10 mm thick AISI 304 build plates of 50 × 50 mm^2 (plate$_{50}$) and 100 × 100 mm^2 (plate$_{100}$) were used. Because of the different plate dimensions, the area exposed to sintering scanning was adapted and set to 80 × 80 mm^2 and 45 × 45 mm^2 for plate$_{100}$ and plate$_{50}$, respectively. The pre-sintering, *i.e*., the heating of the build plate before process start was performed with a nominal current of 15 mA to reach a level of 400 °C and hold this temperature for 10 minutes. Afterwards, the powder was spread in layers of 50 μm

C.J.J. TORRENT, P. KROOSS, and T. NIENDORF are with the Institute of Materials Engineering, University of Kassel, 34125 Kassel, Germany. Contact e-mail: torrent@uni-kassel.de

Manuscript submitted June 17, 2021; accepted October 28, 2021.
Article published online November 17, 2021.

thickness, pre-heated with 12 mA in 15 repetitions, and molten with a beam current of 12.25 mA, a speed of 4000 mm s^{-1}, and a hatch distance of 80 μm. The temperature was measured by a thermocouple (type K) attached directly underneath the build plate. For the present investigations, specimens were extracted from cuboids of 10 × 10 × 40 mm^3. To minimize inhomogeneous heat accumulation or loss, the cuboids were placed with 10 mm distance from each other, and > 5 mm from the borders of the sintering scan area. To exclude any surface effects and effects being related to the layers built first or last, a layer of 1 mm from the as-built surface was removed on all planes. The gage sections studied in the microstructural investigations as well as the gage length of the tensile test specimens are characterized by a distance > 9 mm to the top and bottom of the initial cuboid (*cf.* insets in Figure 1). Electron backscatter diffraction (EBSD) measurements were performed at a nominal voltage of 20 kV. For computed tomography (μ-CT) analysis, a nominal voltage of 140 kV and a nominal current of 10 mA were used, and a specimen volume of ≈ 3.35 mm^3 was probed considering a voxel size of 1.85 μm^3. For the tensile tests, specimens with a cross section of 1.5 × 3 mm^2 (*cf.* Figure 4) were extracted by electrical discharge machining and tested in displacement control with the loading direction parallel to the build direction. Strains up to 30 pct were determined via an extensometer directly attached to the specimen surface. Above this value, strains were calculated from the displacement signal. Hardness was determined applying a load of 9.8 N (HV1) for 10 seconds at 21 positions per specimen. For a more detailed insight into the manufacturing process as well as the analysis methods, the reader is referred to Reference 14.

Figure 1 shows the temperature profile for the two considered processes ($plate_{50}$ and $plate_{100}$) as extracted from the log-files of the E-PBF system. The $plate_{100}$ process is characterized by a slightly longer build time due to the increased number of specimens compared to the $plate_{50}$ process and, due to the simultaneously build cylinders, an increased build height. Keeping all process parameters constant except the size of the build plate and the sintering area, a differing thermal evolution is obvious. During the pre-sintering procedure (initial heating of the build plate up to the point highlighted by the vertical dashed line in Figure 1), the temperature of 400 °C is not maintained, instead a significant overshooting is obvious. Finally, the temperature difference at the beginning of the actual build process (dashed line) is about 270 °C. The reason for this effect is seen in a higher heating rate during pre-sintering in the case of $plate_{50}$. Here, the ratio of the scanned surface to plate size is 0.81, while for $plate_{100}$, the value is 0.64, this difference eventually leading to discrepancies in heating efficiency and homogeneity. Obviously, applying constant heating parameters to differing build plate volumes and weights, respectively, results in unequal

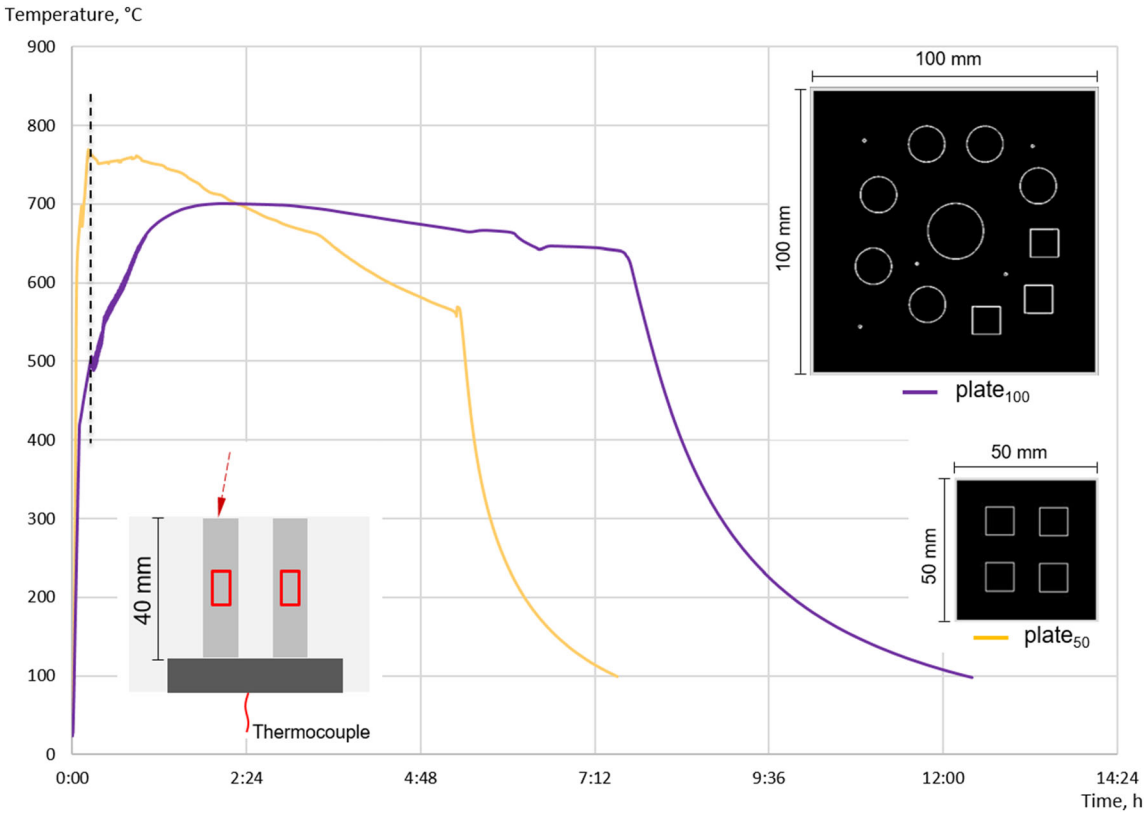

Fig. 1—Temperature profiles of the two processes including a schematic detailing the build layout. Microstructure analysis and mechanical testing were performed in the center of the built cuboids (highlighted by red rectangles) (Color figure online).

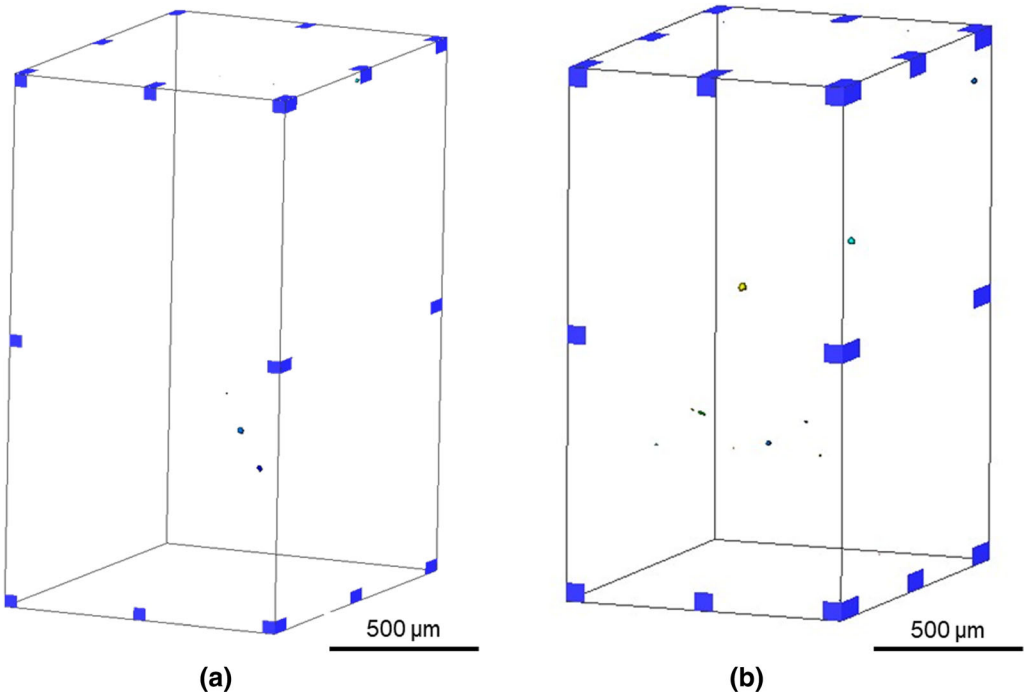

Fig. 2—μ-CT measurement of a representative specimen volume built on the 100 × 100 mm^2 platform in (*a*) and 50 × 50 mm^2 platform in (*b*) (a partly recompiled from Ref. [14] under the terms of CC BY-NC-ND license).

temperature evolution. The input power P is the product of beam current I and voltage U. Power can also be related to the temperature change ΔT of a body of the weight m and specific heat capacity c in a certain time span t, being also captured by the heating power $\dot{Q}$:

$$P = U \cdot I = \frac{m \cdot c \cdot \Delta T}{t} = \dot{Q}. \quad [1]$$

Since U and I are equal in both process runs considered, the heating power introduced to plate$_{100}$ and plate$_{50}$ is also equal:

$$\frac{m_{100} \cdot c \cdot \Delta T_{100}}{t_{100}} = \frac{m_{50} \cdot c \cdot \Delta T_{50}}{t_{50}}. \quad [2]$$

Being of the same material, the specific heat capacity c is equal for both build plates. Further, based on the above mentioned dimensions, the weight of plate$_{100}$ is four times that of plate$_{50}$. Thus, Eq. [2] can be expressed as follows:

$$\frac{4 \cdot \Delta T_{100}}{t_{100}} = \frac{\Delta T_{50}}{t_{50}}. \quad [3]$$

From this equation, it can be deduced that in the same time span $t_{100} = t_{50}$, the smaller build plate$_{50}$ is heated more severely, *i.e.*, by a factor of four compared to plate$_{100}$. This simplistic consideration does not consider different heat losses via radiation or contact to the powder bed in dependence of the build plate surface. Further, parameters in the control software counteracting overshooting (being enabled in both processes) are not taken into account. Still, from this simplistic model it is obvious that independent from the scanning area and strategy, plate$_{50}$ is heated more effectively than the larger plate$_{100}$ in a given time interval. During the subsequent build process, in which the scanned area and layer time are smaller, the energy input is lower for plate$_{50}$, leading in turn to a faster temperature decrease in comparison to plate$_{100}$. Here, the pre-heating process, *i.e.*, the heating of the deposited powder before melting is performed as a function of number of repetitions and not in relation to the absolute time value entered into the control software. Thus, pre-sintering scales with the smaller scanning area. In addition, a significantly smaller amount of sintered powder, as is the case for plate$_{50}$, is expected to promote a more pronounced loss of thermal energy over time compared to plate$_{100}$. Again, except for the scanned surface, the parameters for the pre-sintering procedure were kept constant for both build processes compared in present work. As a function of different scanning areas for heating and melting in the two processes, layer times are 117 and 52 s for plate$_{100}$ and plate$_{50}$, respectively. This is thought to cause a steeper temperature decrease over the build height for the plate$_{50}$ process in comparison to the plate$_{100}$ process, maintaining a more constant temperature level in case of the latter. Since the temperature is recorded underneath the build plate in ARCAM A2X machines, the real temperature at a specific layer remains unknown during processing, however, being obviously higher as the recorded and plotted absolute temperature. Furthermore, the local temperature evolution in a specific volume increment is supposed to alternate significantly as result of the local, high, and rapid energy input. Both the higher absolute temperature and the rapidly alternating local temperature evolution are not apparent from the thermocouple

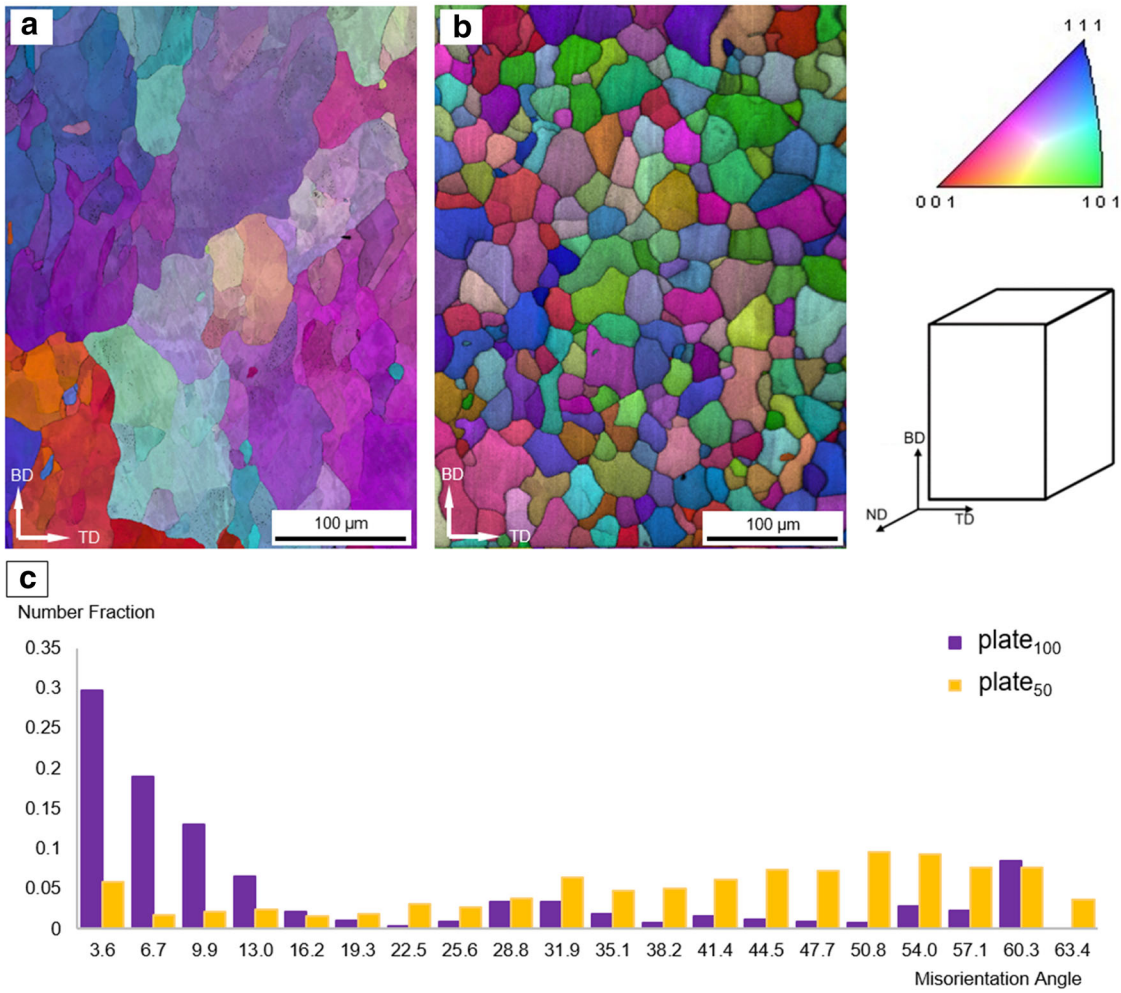

Fig. 3—EBSD orientation maps for specimens processed on $plate_{100}$ (*a*) and $plate_{50}$ (*b*) (indexed for normal direction (ND)) and misorientation angle distribution (*c*) (a and c partly recompiled from Ref. [14] under the terms of CC BY-NC-ND license).

signal since thermal conditions homogenize during the ongoing build process. Anyhow, a significant impact on the resulting properties is to be expected.

The μ-CT measurements shown in Figure 2 reveal a similar relative density of > 99.9 pct for the different sets of specimens. Severe lack of fusion and/or keyholing caused by different temperature levels are not detectable in the probed volumes. The average sphericity of the pores is > 0.9 at an average diameter of about 8 μm. Based on studies reporting on the formation of pores in PB-AM, the small and spherical pores are supposed to stem from gas entrapments in the atomized powder feedstock.[15–17]

However, a significant difference is found in the microstructure appearance shown in Figure 3. While the material processed on $plate_{50}$ (Figure 3b) is characterized by a predominantly globular microstructure, the $plate_{100}$ specimens (Figure 3a) show irregularly shaped and coarser grains (as already shown in Reference 14). Further, the grain boundaries in the $plate_{100}$ processed iron are mostly of low-angle character, as can be seen in Figure 3c, where the misorientation is plotted versus the number fraction. Considering every misorientation of more than 2 deg, the $plate_{50}$ condition has a 150 pct higher boundary density than the $plate_{100}$ state (calculated by the OIM software).

In most E-PBF parameter studies, the appearance of the final microstructure is correlated to prevailing thermal conditions in dependence of the energy input,[1,6,18] to effects promoted by pores[4] as well as secondary phases.[19] As detailed before, except the build envelope size and, in consequence, the processing area, all process parameters were kept constant in present work. Since the density and character of pores of the two investigated cp-Fe conditions are very similar in the probed volumes, a significant impact of those on the different microstructures presented can be neglected.

With respect to the local thermal path and intrinsic heat treatment, respectively, results presented in References 12, 13, and 20 indicate that multiple solid–to-solid phase transformations can occur in PB-AM, eventually depending on the processed alloy. In the case of laser-based powder bed fusion (L-PBF), thermal and phase transformation-induced internal stresses can promote formation of subgrain structures.[20] This is not expected in the present study as the high temperature

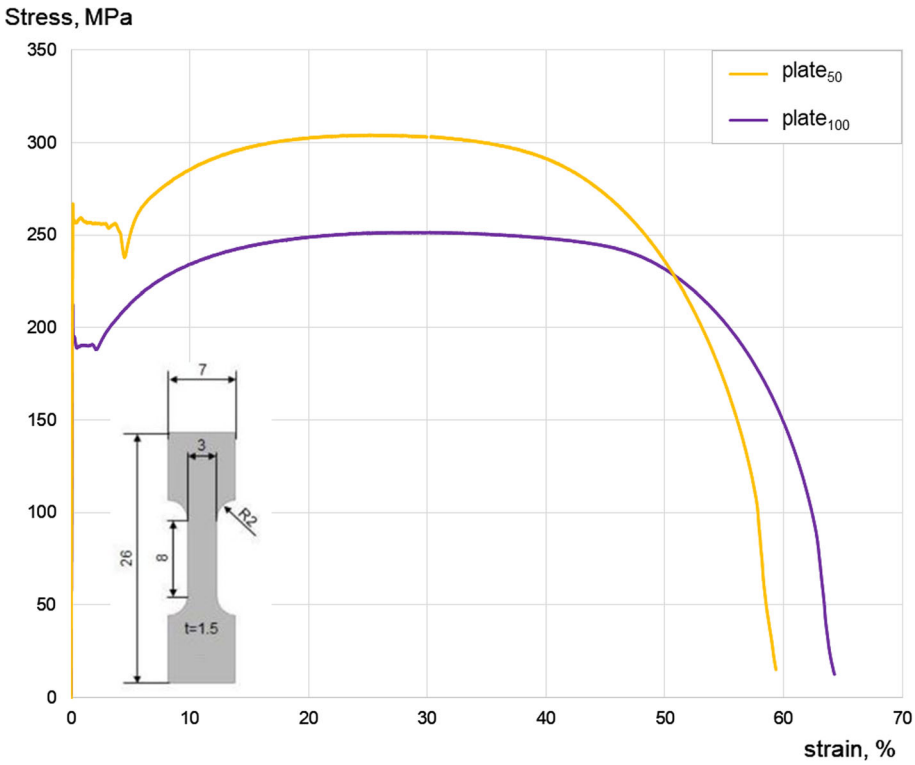

Fig. 4—Stress–strain curves for $plate_{100}$ and $plate_{50}$ processed E-PBF cp-Fe specimens (partly recompiled from Ref. [14] under the terms of CC BY-NC-ND license).

level in E-PBF is known to lead to relatively low residual stress values. In cp-Fe, a phase transition takes place at about 911 °C, whereby 24 α variants (according to Kurdjmov–Sachs[21]) can originate from one γ crystal. Consequently, at elevated process temperatures (in the case of $plate_{50}$), multiple $\alpha \leftrightarrow \gamma$ phase transformations promote a refinement of initially larger grains (established during solidification; transition path: liquid $\rightarrow \delta \rightarrow \gamma \rightarrow \alpha$) leading to the final microstructure shown in Figure 3b. In contrast, if a generally lower thermal level prevails (as in case of $plate_{100}$), then multiple phase transformation events are hampered and, eventually, related effects are inhibited. In consequence, the microstructure is fragmented, however, not fully recrystallized, and LAGBs dominate the final microstructure appearance (Figure 3a) and mechanical properties, respectively, as will be discussed in the next paragraph. This argumentation is supported by the quantitative analysis of the high fraction of LAGBs (*cf.* Figure 3c) in the $plate_{100}$ material. Recovery most significantly contributes to final microstructure appearance in this case, *i.e.*, high fractions of high-angle grain boundaries (HAGBs) induced by multiple phase transformations did not form.

The stress–strain curves shown in Figure 4 reveal differing mechanical responses of the two microstructures, *i.e.*, $plate_{50}$ and $plate_{100}$ E-PBF cp-Fe. The $plate_{50}$ specimen shows a higher yield strength (YS) and ultimate tensile strength (UTS). This fact can be rationalized based on the Hall–Petch relation, taking into account the differences in grain boundary character depicted in Figure 3 as will be detailed in the following. For both the YS (267 MPa for $plate_{50}$ and 212 MPa for $plate_{100}$) and the UTS (304 MPa and 248 MPa, respectively) values are 20 pct higher in the $plate_{50}$ material. The $plate_{100}$ microstructure promotes a higher elongation at fracture of 64 pct. The hardness values are similar, *i.e.*, 88.7 HV1 and 83.6 HV1 for the $plate_{50}$ and $plate_{100}$ conditions, respectively.

These results are in good agreement with the microstructures depicted in Figure 3: a microstructure dominated by LAGBs, as in case of the $plate_{100}$ specimen, allows for more intense dislocation activity. While the difference in elongation at fracture is less pronounced, differences in YS and UTS are significant. Eventually, the higher strength in the $plate_{50}$ material can be attributed to the HAGB-dominated microstructure, eventually contributing to a more efficient grain boundary strengthening.

In conclusion, the present paper demonstrates that minor deviations in processing conditions, being often not considered in evaluation of results, can have a pronounced impact on the properties of PB-AM processed materials. As revealed by data presented, differences in process temperature can significantly influence microstructure evolution. In this regard, the build plate size has a significant impact on the process temperature evolution as long as the input power is not adapted. As a consequence, the general process temperature increases to a level promoting multiple phase transformations in the cp-Fe considered in present work. Eventually, these transformation events lead to significant grain

refinement. The different microstructural appearances stemming from the slightly differing process temperatures can lead to a significant difference in strength. Thus, principally tailoring microstructures of E-PBF products is possible; however, process conditions have to be exactly controlled for this purpose. The calculation of the true temperature course on the build plate as well as in the whole build volume is not trivial. A complete description of the interrelations between heating power coupling, electron dissipation, change of thermal and electrical conductivity, and power regulation, inter alia, still is missing. Furthermore, the number, position, build layout, *etc*., of parts in a build process are known to also have an effect on the thermal distribution and history, respectively. Such aspects, as well as the behavior of the two presented microstructures under cyclic loading, will have to be addressed in future studies.

ACKNOWLEDGMENTS

This work was supported by Deutsche Forschungsgemeinschaft (DFG) under Grant 413259151.

CONFLICT OF INTEREST

On behalf of all authors, the corresponding author states that there is no conflict of interest.

FUNDING

Open Access funding enabled and organized by Projekt DEAL.

OPEN ACCESS

REFERENCES

1. R.R. Dehoff, M.M. Kirka, W.J. Sames, H. Bilheux, A.S. Tremsin, L.E. Lowe, and S.S. Babu: *Mater. Sci. Technol.*, 2015, vol. 31, pp. 931–38.
2. N. Raghavan, R. Dehoff, S. Pannala, S. Simunovic, M. Kirka, J. Turner, N. Carlson, and S.S. Babu: *Acta Mater.*, 2016, vol. 112, pp. 303–14.
3. T. Scharowsky, A. Bauereiß, and C. Körner: *Int. J. Adv. Manuf. Technol.*, 2017, vol. 92, pp. 2809–18.
4. X. Ding, Y. Koizumi, K. Aoyagi, T. Kii, N. Sasaki, Y. Hayasaka, K. Yamanaka, and A. Chiba: *Mater. Sci. Eng. A*, 2019, vol. 764, p. 138058.
5. C. Körner, H. Helmer, A. Bauereiß, and R.F. Singer: *MATEC Web Conf.*, 2014, vol. 14, p. 8001.
6. N. Raghavan, S. Simunovic, R. Dehoff, A. Plotkowski, J. Turner, M. Kirka, and S. Babu: *Acta Mater.*, 2017, vol. 140, pp. 375–87.
7. G.S. Altug-Peduk, S. Dilibal, O. Harrysson, S. Ozbek, and H. West: *Russ. J. Non-ferr. Met.*, 2018, vol. 59, pp. 433–39.
8. L.C. Ardila, F. Garciandia, J.B. González-Díaz, P. Álvarez, A. Echeverria, M.M. Petite, R. Deffley, and J. Ochoa: *Phys. Procedia*, 2014, vol. 56, pp. 99–107.
9. F. Brenne and T. Niendorf: *Int. J. Fatigue*, 2019, vol. 127, pp. 175–89.
10. S. Goel, J. Olsson, M. Ahlfors, U. Klement, and S. Joshi: in *Proceedings of the 9th International Symposium on Superalloy 718 and Derivatives: Energy, Aerospace, and Industrial Applications*, E. Ott, X. Liu, J. Andersson, Z. Bi, K. Bockenstedt, I. Dempster, J. Groh, K. Heck, P. Jablonski, M. Kaplan, D. Nagahama, and C. Sudbrack, eds., Springer, Cham, 2018, pp. 115–29.
11. D. Kotzem, T. Arold, T. Niendorf, and F. Walther: *Mater. Sci. Eng. A*, 2020, vol. 772, p. 138785.
12. J. Günther, F. Brenne, M. Droste, M. Wendler, O. Volkova, H. Biermann, and T. Niendorf: *Sci. Rep.*, 2018, vol. 8, p. 1298.
13. C. Körner: *Int. Mater. Rev.*, 2016, vol. 61, pp. 361–77.
14. C.J.J. Torrent, S. Wackenrohr, R. Richter, C.E. Sobrero, S. Degener, P. Krooß, H.J. Maier, and T. Niendorf: *Adv. Eng. Mater.*, 2021, vol. 327, p. 2100018.
15. S.M. Gaytan, L.E. Murr, F. Medina, E. Martinez, M.I. Lopez, and R.B. Wicker: *Mater. Technol.*, 2009, vol. 24, pp. 180–90.
16. S. Tammas-Williams, H. Zhao, F. Léonard, F. Derguti, I. Todd, and P.B. Prangnell: *Mater. Charact.*, 2015, vol. 102, pp. 47–61.
17. G. Chen, Q. Zhou, S.Y. Zhao, J.O. Yin, P. Tan, Z.F. Li, Y. Ge, J. Wang, and H.P. Tang: *Powder Technol.*, 2018, vol. 330, pp. 425–30.
18. H. Helmer, A. Bauereiß, R.F. Singer, and C. Körner: *Mater. Sci. Eng. A*, 2016, vol. 668, pp. 180–87.
19. H. Bian, K. Aoyagi, Y. Zhao, C. Maeda, T. Mouri, and A. Chiba: *Addit. Manuf.*, 2020, vol. 32, p. 100982.
20. P. Lejček, M. Roudnická, J. Čapek, D. Dvorský, J. Drahokoupil, D. Šimek, J. Čížek, P. Svora, O. Molnárová, and D. Vojtěch: *Mater. Charact.*, 2019, vol. 154, pp. 222–32.
21. G. Kurdjumow and G. Sachs: *Z. Phys.*, 1930, vol. 64, pp. 325–43.